






## Anomalous Nernst effect and topological Nernst effect in the ferrimagnetic nodal-line semiconductor $\text{Mn}_3\text{Si}_2\text{Te}_6$

Chen Ran <sup>1,\*</sup>, Xinrun Mi <sup>1,\*</sup>, Junying Shen <sup>2,3,\*</sup>, Honghui Wang,<sup>1</sup> Kunya Yang,<sup>1</sup> Yan Liu,<sup>4</sup> Guiwen Wang,<sup>4</sup> Guoyu Wang <sup>5</sup>, Youguo Shi,<sup>6</sup> Aifeng Wang,<sup>1</sup> Yisheng Chai,<sup>1</sup> Xiaolong Yang <sup>1</sup>, Mingquan He <sup>1,†</sup>, Xin Tong,<sup>2,3,‡</sup> and Xiaoyuan Zhou<sup>1,§</sup>

<sup>1</sup>College of Physics & Center of Quantum Materials and Devices, Chongqing University, Chongqing 401331, People's Republic of China

<sup>2</sup>Institute of High Energy Physics, Chinese Academy of Sciences (CAS), Beijing 100049, People's Republic of China

<sup>3</sup>Spallation Neutron Source Science Center, Dongguan 523803, People's Republic of China

<sup>4</sup>Analytical and Testing Center, Chongqing University, Chongqing 401331, People's Republic of China

<sup>5</sup>Center of Quantum Materials and Devices, Chongqing University, Chongqing 401331, People's Republic of China

<sup>6</sup>Beijing National Laboratory for Condensed Matter Physics and Institute of Physics, Chinese Academy of Sciences, Beijing 100190, People's Republic of China



(Received 27 February 2023; revised 7 August 2023; accepted 22 August 2023; published 1 September 2023)

In the ferrimagnetic nodal-line semiconductor  $\text{Mn}_3\text{Si}_2\text{Te}_6$ , colossal magnetoresistance (CMR) arises below  $T_c = 78$  K due to the interplay of magnetism and topological nodal-line electronic structures. Here, we present electrical and thermoelectric transport properties of  $\text{Mn}_3\text{Si}_2\text{Te}_6$ . Below  $T_c$ , the Nernst signal is dominated by anomalous Nernst effect (ANE) in the high-field region above 3 T. The scaling ratio between the ANE and magnetization is comparable to that in conventional magnetic materials, suggesting minor contributions from the nodal-line structure. In the low-field region ( $0 \sim 3$  T) where the CMR is most apparent, possible signatures of topological Nernst effect (TNE) are found, which are likely associated with the noncollinear magnetic structure.

DOI: [10.1103/PhysRevB.108.125103](https://doi.org/10.1103/PhysRevB.108.125103)

### I. INTRODUCTION

In magnetic topological materials, the interplay of magnetism and band topology often gives rise to a variety of nontrivial transport properties, such as giant anomalous Hall effect (AHE), giant anomalous Nernst effect (ANE) and quantum anomalous Hall effect [1–6]. The intimate coupling between spin degrees of freedom and electronic band topology allows easy manipulation of spin or charge transport by tailoring spin configurations using external magnetic fields. The peculiar transport effects together with their easy tunability in magnetic topological materials are highly favored in developing magnetoelectric, spintronic device applications.

Of particular interest is the ferrimagnetic nodal-line semiconductor  $\text{Mn}_3\text{Si}_2\text{Te}_6$ , which displays colossal magnetoresistance (CMR) in the ferrimagnetic state [7–10]. As shown in Fig. 1(a),  $\text{Mn}_3\text{Si}_2\text{Te}_6$  is a van der Waals layered material, which crystallizes in a trigonal structure (space group:  $P\bar{3}1c$ , No. 163). There are two types of Mn atoms. The Mn1 atoms and Te atoms form edge sharing  $\text{MnTe}_6$  octahedra, creating honeycomb layers within the  $ab$  plane. The Mn2 atoms are sandwiched by the Mn1 layers, forming a triangular pattern. Below  $T_c \sim 78$  K,  $\text{Mn}_3\text{Si}_2\text{Te}_6$  enters a ferrimagnetic state, in which Mn1 layers and Mn2 layers are bonded antiferromagnetically [11–13]. A recent neutron diffraction study

revealed a noncollinear magnetic structure with the moment directions oriented  $\sim 10^\circ$  away from the easy  $ab$  plane [see Fig. 1(a)] [13]. The noncollinearity is seen more clearly in the projected view along the  $c$  axis, as shown in the bottom left panel in Fig. 1(a). In the ferrimagnetic state, negative CMR reaching up to nine orders of magnitude appears only when an external magnetic field is directed along the magnetic hard  $c$  axis, in contrast to conventional CMR materials [7–9]. Only moderate negative magnetoresistance is found when a magnetic field is applied within the magnetic easy  $ab$  plane, leading to colossal angular magnetoresistance up to  $\sim 10^{11}\%$  per radian [9]. It has been suggested that the CMR arises from an insulator-metal transition, which is induced by lifting the spin orientation-dependent nodal-line band degeneracy [9,14]. As illustrated schematically in the right panels of Fig. 1(a), the bandgap depends strongly on the spin orientations. When the spins are lying within the  $ab$  plane ( $M \parallel a$ ), a finite bandgap is seen and a twofold degenerate nodal-line structure appears at the  $\Gamma$  point in the spin-polarized Te valence bands [9,14]. The nodal-line degeneracy is lifted by aligning the moments along the  $c$  axis ( $M \parallel c$ ) [9,14]. As a result, the bandgap is closed, leading to a metallic state in the  $M \parallel c$  polarized state [9,14]. Alternatively, chiral orbital currents (COC) may emerge within the  $ab$  plane, producing orbital magnetic moments oriented along the  $c$  axis [8]. These orbital magnetic moments and COC domains interact strongly with the Mn moments, giving rise to negative CMR by aligning the COC domains in a  $c$ -axis magnetic field [8]. Still, the nature of the observed unusual CMR in  $\text{Mn}_3\text{Si}_2\text{Te}_6$  remains elusive.

When the topological nodal-line degeneracy is lifted, finite Berry curvature arises near the Fermi level [9]. Consequently,

\*These authors contributed equally to this work.

<sup>†</sup>mingquan.he@cqu.edu.cn

<sup>‡</sup>tongx@ihep.ac.cn

<sup>§</sup>xiaoyuan2013@cqu.edu.cn

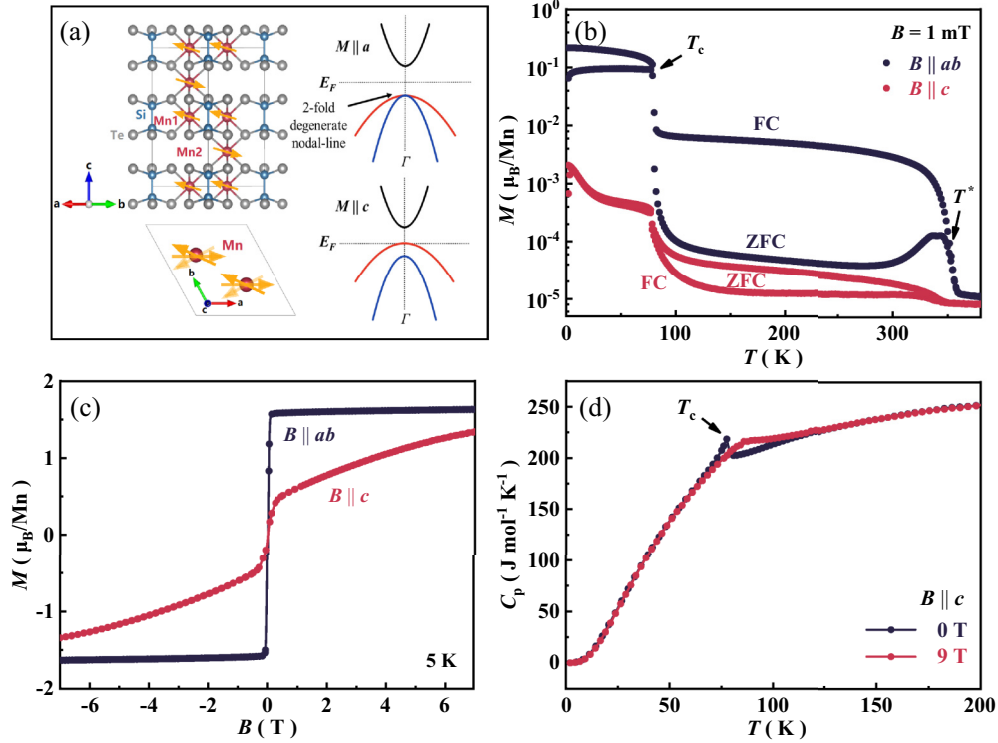


FIG. 1. (a) Upper left: crystal structure of Mn<sub>3</sub>Si<sub>2</sub>Te<sub>6</sub> (side view) [13]. Arrows on Mn atoms represent magnetic moments which order ferrimagnetically below  $T_c = 78$  K. Bottom left: top view of the noncollinear magnetic structure. Upper right and bottom right: schematic band structures for  $M \parallel a$  and  $M \parallel c$ , respectively [9,14]. (b) Temperature dependence of magnetization  $M(T)$  for a Mn<sub>3</sub>Si<sub>2</sub>Te<sub>6</sub> single crystal. Both zero-field-cooled (ZFC) and field-cooled (FC) results with a magnetic field  $B = 1$  mT applied within the  $ab$  plane and along the  $c$  axis are shown. In addition to the ferrimagnetic transition at  $T_c$ , another transition is also seen at  $T^*$ . (c) Isothermal magnetization  $M(H)$  measured at  $T = 5$  K. (d) Temperature-dependent specific heat  $C_p(T)$  captured in 0 and 9 T.

other intriguing transport properties may also appear, such as the AHE and ANE [15,16]. In particular, the ANE is extremely sensitive to the Berry curvatures close to the Fermi energy ( $E_F$ ) as the ANE probes the energy derivative of charge transport at  $E_F$  [15,16]. Indeed, Berry curvature-induced large ANE has been observed in various magnetic topological semimetals, such as Co<sub>3</sub>Sn<sub>2</sub>S<sub>2</sub> [17–19], Co<sub>2</sub>MnGa [20–22], Mn<sub>3</sub>Sn [2,23], Fe<sub>3</sub>Sn<sub>2</sub> [24,25], and Fe<sub>3</sub>GeTe<sub>2</sub> [26]. In this report, we probe the Berry curvature associated with the nodal-line structure in Mn<sub>3</sub>Si<sub>2</sub>Te<sub>6</sub> using thermoelectric Seebeck and Nernst measurements. Sizable ANE which peaks around  $T_c$  is found in magnetic fields applied along the  $c$  axis. However, unlike other magnetic topological materials, the magnetization-induced ANE falls close to the typical region covered by conventional magnets, pointing to subdominant roles played by the nodal-line band topology. In addition to the ANE, topological Nernst effect (TNE) also arises below  $T_c$  in small magnetic fields below 3 T. Importantly, the CMR is also predominantly achieved within 3 T. The observed TNE-like signal in Mn<sub>3</sub>Si<sub>2</sub>Te<sub>6</sub> is likely produced by the noncollinear spin texture, which may also have intimate correlation with the CMR.

## II. EXPERIMENTAL METHODS

Single crystals of Mn<sub>3</sub>Si<sub>2</sub>Te<sub>6</sub> were grown using the flux method [9]. Starting materials of Mn, Si, and Te were mixed in

a molar ratio of 3:2:12 in Ar atmosphere. The mixed materials were then placed in an alumina crucible and sealed in an evacuated quartz tube. The tube was first heated in a muffle furnace to 1000 °C and dwelt for 20 h. Then the furnace was slowly cooled to 750 °C at a rate of 1.5 °C/h. The tube was quickly taken out of the furnace, and Mn<sub>3</sub>Si<sub>2</sub>Te<sub>6</sub> single crystals with typical dimensions of 5 × 5 × 1 mm<sup>3</sup> were finally obtained after removing the flux by centrifugation.

The crystal structure of Mn<sub>3</sub>Si<sub>2</sub>Te<sub>6</sub> crystals was characterized by single crystal diffraction experiments using a Bruker D8 venture diffractometer (see the Supplemental Material [27]). The magnetic properties were measured in a magnetic properties measurement system (MPMS-3, Quantum Design Inc.). Resistivity and Hall resistivity were performed in a physical property measurement system (PPMS DynaCool 9 T, Quantum Design Inc.) using a standard Hall-bar geometry. The longitudinal and transverse thermoelectric measurements were carried out in a cryostat (TESPT14T50, Oxford Instruments inc.) using a home-built setup equipped with one heater and two thermometers.

## III. RESULTS AND DISCUSSION

In Fig. 1(b), we present the temperature dependence of magnetization for a Mn<sub>3</sub>Si<sub>2</sub>Te<sub>6</sub> single crystal. The ferrimagnetic transition is seen clearly at  $T_c = 78$  K, agreeing well with other reports [7–11]. Below  $T_c$ , the in-plane magneti-

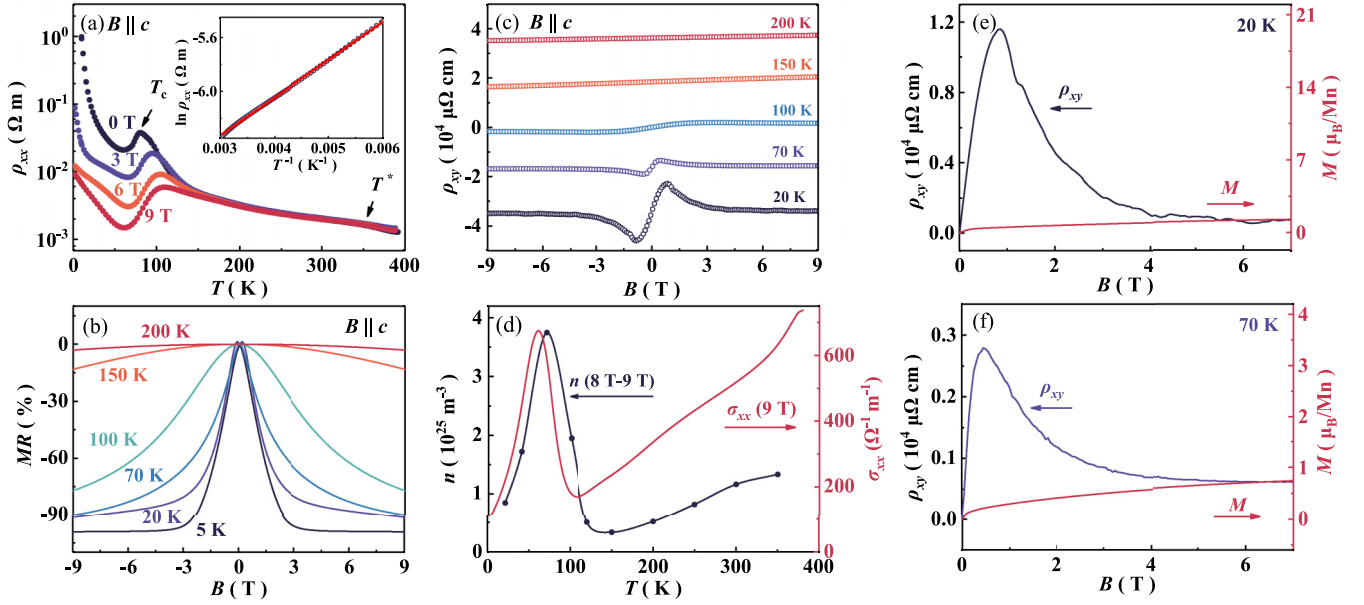


FIG. 2. (a) Temperature dependence of in-plane resistivity  $\rho_{xx}$  measured with magnetic fields applied along the  $c$  axis. The inset in (a) shows the fitting (red line) of resistivity between 150 K and 300 K using a thermally activated model. (b) The magnetoresistance  $MR = [\rho_{xx}(B) - \rho_{xx}(0)]/\rho_{xx}(0)$  measured at different temperatures with  $B \parallel c$ . (c) The Hall resistivity  $\rho_{xy}$  recorded at selective temperatures. Vertical offsets have been applied for clarity. (d) Estimated carrier density ( $n$ ) using the high-field Hall resistivity measured between 8 and 9 T. The electrical conductivity ( $\sigma_{xx}$ ) measured in 9 T is also plotted for comparison. (e) and (f) Comparison of the Hall resistivity and magnetization recorded at 20 and 70 K.

zation ( $B \parallel ab$ ) is two orders of magnitude larger than that of out-of-plane ( $B \parallel c$ ), in accordance with an in-plane easy axis [see Fig. 1(a)]. Note that this easy-plane anisotropy appears already above  $T_c$  and persists up to  $T^* \sim 350$  K, above which the paramagnetic state is recovered. The transition at  $T^*$  is consistently seen in melt-grown crystals [7,11,28], but disappears in samples prepared by the vapor transport method [29]. The nature of the transition at  $T^*$  is still not clear, and may originate from short-range ordering [11]. The strong magnetic anisotropy in the ferrimagnetic state can be further revealed by isothermal magnetization measurements, as shown in Fig. 1(c). The magnetization saturates rapidly to  $\sim 1.6 \mu_B/\text{Mn}$  in a weak magnetic field of 0.1 T for  $B \parallel ab$ . For  $B \parallel c$ , on the other hand, a strong magnetic field up to 7 T cannot fully polarize the magnetic moments (see more data in the Supplemental Material [27]). The field anisotropy is found to be as large as 13 T [7].

The temperature dependence of specific heat ( $C_p$ ) of  $\text{Mn}_3\text{Si}_2\text{Te}_6$  is plotted in Fig. 1(d). In zero magnetic field, the ferrimagnetic transition is manifested as a  $\lambda$ -shaped peak at  $T_c$ . The transition is smeared out in the presence of magnetic fields and shifts gradually toward higher temperatures due to the suppression of magnetic fluctuations. Above 150 K,  $C_p$  recorded in 0 and 9 T coincides. This indicates that magnetic fluctuations appear well above  $T_c$  and survive to about 150 K. Short-range spin fluctuations may already develop below  $T^*$ , as suggested by neutron scattering and Raman spectroscopy experiments [11–13,30].

Figure 2 shows electrical transport results of a  $\text{Mn}_3\text{Si}_2\text{Te}_6$  single crystal. As shown in Fig. 2(a), the in-plane resistivity  $\rho_{xx}$  increases rapidly with cooling, pointing to a semiconducting nature. Within 150–300 K,  $\rho_{xx}(T)$  measured in 0 T follows

a thermally activated model  $\rho_{xx}(T) = \rho_0 \exp(\Delta/k_B T)$ , with an activation energy  $\Delta = 24.3(1)$  meV [see the inset in Fig. 2(a)], in agreement with other reports [9,11,14]. Here,  $k_B$  is the Boltzmann constant, and  $\rho_0$  is a material-dependent constant. Further cooling below 150 K,  $\rho_{xx}(T)$  deviates from the simple activation behavior due to increasing scattering of carriers by sizable spin fluctuations. Establishment of long-range ferrimagnetic order below  $T_c$  strongly suppresses magnetic fluctuations, leading to a clear drop in  $\rho_{xx}$  when passing through  $T_c$  upon cooling. Note that the transition at  $T^*$  appears as a broad hump in resistivity.

The most notable feature of  $\text{Mn}_3\text{Si}_2\text{Te}_6$  is the negative CMR. As seen in Figs. 2(a) and 2(b),  $\rho_{xx}$  is significantly reduced in the presence of out-of-plane magnetic fields below 150 K. The negative CMR becomes particularly evident at lower temperatures. At 5 K,  $MR = [\rho_{xx}(B) - \rho_{xx}(0 \text{ T})]/\rho_{xx}(0 \text{ T})$  reaches  $-99.2\%$  in 9 T. Note that the CMR is most profound in the low-field region below 3 T. Intriguingly, the CMR only appears when a magnetic field is applied along the magnetic hard axis ( $B \parallel c$ ) [7,9]. The coupling between spin orientation and nodal-line degeneracy and/or chiral orbital currents have been invoked to explain the CMR in  $\text{Mn}_3\text{Si}_2\text{Te}_6$  [8,9]. The underlying mechanisms of the observed CMR remain to be elucidated.

The Hall resistivity  $\rho_{xy}$  measured at various temperatures is displayed in Fig. 2(c) (see the Supplemental Material for more data measured at other temperatures [27]). Above 150 K,  $\rho_{xy}(B)$  scales linearly with magnetic field with positive slopes, which suggests that the electrical transport is dominated by holelike carriers. Nonlinear magnetic field dependence of  $\rho_{xy}(B)$  develops below 150 K, which resembles multiband transport behaviors at the first glance. However, the negative

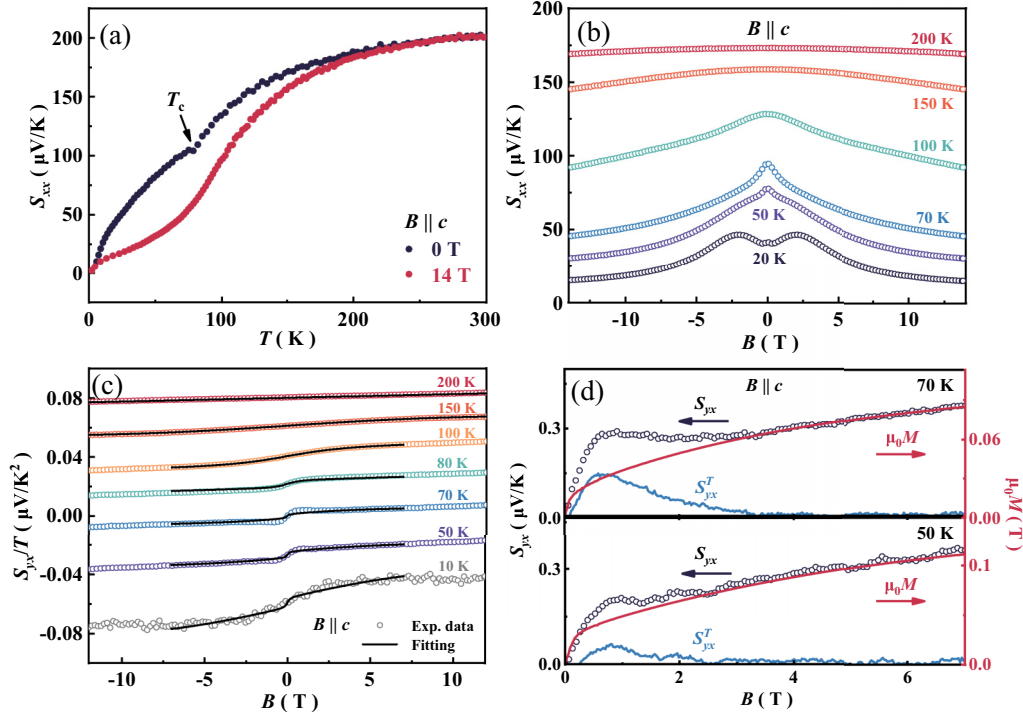


FIG. 3. (a) Temperature dependence of the in-plane Seebeck coefficient  $S_{xx}$  measured in  $B = 0$  T and 14 T applied along the  $c$  axis. (b) Magneto-Seebeck effect  $S_{xx}(B)$  measured at various temperatures. (c) The Nernst effect  $S_{yx}/T$  measured at fixed temperatures. Curves have been shifted vertically for clarity. Solid black lines are fitting of the Nernst signal according to Eq. (1). (d) Scaling between the Nernst signal  $S_{yx}(B)$  and magnetization  $M$  measured at 50 and 70 K. The TNE-like component ( $S_{yx}^T$ ) is obtained after subtracting the anomalous part from the total Nernst data.

magnetoresistance<sup>2</sup> observed below 150 K cannot be described by a simple multiband scenario. In addition, the bandgap is sensitive to the spin orientations as well as external magnetic fields. As a result, the carrier concentration also depends on the strength of external magnetic fields. In high magnetic fields, the resistivity is weakly field-dependent [see Fig. 2(b)]. It is thus possible to extract the carrier density in the high-field region. The estimated carrier density ( $n$ ) using the Hall resistivity measured between 8 and 9 T is presented in Fig. 2(d). Clearly, the temperature dependence of the estimated carrier concentration nicely tracks the temperature-dependent conductivity ( $\sigma_{xx}$ ) recorded in 9 T. Therefore, this simple estimation gives a good approximation to the carrier density in the high-field region. Similar temperature-dependent carrier concentration has also been estimated in an earlier report [7].

Below  $T_c$ ,  $\rho_{xy}(B)$  rises rapidly in small magnetic fields, which may contain contributions from the AHE, as also suggested by a previous study [7]. In general, the Hall resistivity of a magnetic material can be described as  $\rho_{xy} = \rho_{xy}^0 + \rho_{xy}^A$ , where  $\rho_{xy}^0 = R_0 B$  is the ordinary Hall contribution and  $\rho_{xy}^A = R_S \mu_0 M$  is the AHE term, respectively. Here,  $R_0$  and  $R_S$  are the ordinary and anomalous Hall coefficients, respectively,  $\mu_0$  is the magnetic permeability of free space, and  $M$  is the magnetization. In Figs. 3(e) and 3(f), the Hall resistivity and magnetization measured at 20 and 70 K are directly compared. Clear discrepancies are seen between the Hall resistivity and magnetization in response to external magnetic fields. Even in the high-field region,  $\rho_{xy}$  does not math well with  $M$ . These

results suggest that the AHE alone is not sufficient to account for the total Hall resistivity. Since the magnetization does not become saturated until about 13 T in the  $B \parallel c$  configuration [7], reasonable separation of ordinary and anomalous contributions is beyond the scope of the data measured below 7 T. Moreover, the broad peak in the Hall resistivity appearing in the low-field region cannot be described by considering both the ordinary and anomalous parts. Additional contributions, possibly the topological Hall effect (THE), are involved considering the noncollinear magnetic nature of  $\text{Mn}_3\text{Si}_2\text{Te}_6$  [see Fig. 1(a)]. Although typically seen in skyrmion phases, the THE has been found in various noncollinear magnets, such as  $\text{Mn}_3\text{Sn}$  [31],  $\text{Mn}_3\text{Ga}$  [32], and  $\text{Mn}_5\text{Si}_3$  [33]. Note that the simple form  $\rho_{xy}^0 = R_0 B$  of the ordinary Hall effect may not be valid below  $T_c$  when the pronounced CMR appears in the low-field region. The THE-like Hall data could be induced by the CMR effect, which deserves further study.

In Fig. 3, we present the Seebeck ( $S_{xx}$ ) and Nernst ( $S_{yx}$ ) effects of  $\text{Mn}_3\text{Si}_2\text{Te}_6$ . As seen in Fig. 3(a), the Seebeck signal carries a positive sign all the way from room temperature down to 2 K. This indicates that holelike carriers play dominant roles, agreeing well with the Hall resistivity data. In zero magnetic field,  $S_{xx}$  decreases gradually with cooling and a kink is found at  $T_c$ . Unlike the divergent Seebeck signal reported earlier [28],  $S_{xx}$  observed here approaches zero at low temperatures, in line with the third law of thermodynamics. In 14 T,  $S_{xx}$  is suppressed, which becomes apparent below about 200 K. The magneto-Seebeck effect  $S_{xx}(B)$  is seen

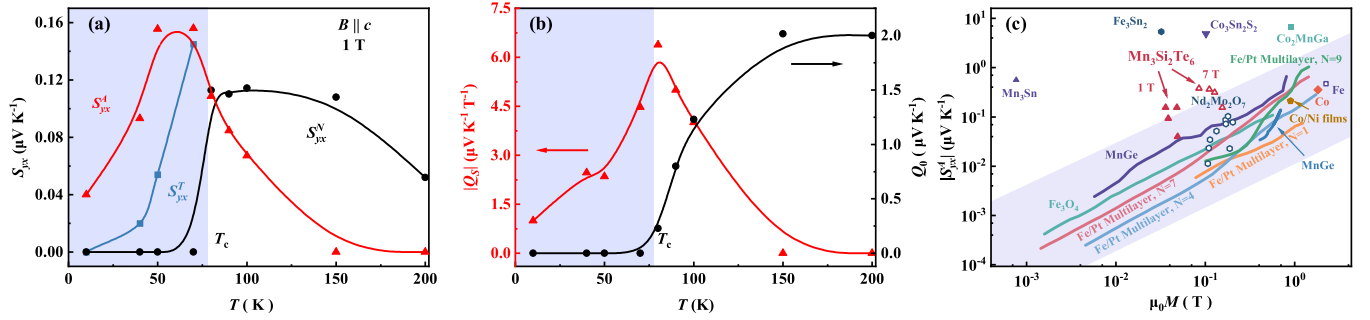


FIG. 4. (a) Temperature dependence of the ordinary ( $S_{yx}^N$ ), anomalous ( $S_{yx}^A$ ), and topological Nernst ( $S_{yx}^T$ ) contributions extracted in a magnetic field of 1 T. (b) Temperature dependence of the ordinary ( $Q_0$ ) and anomalous ( $Q_S$ ) Nernst coefficients. Lines in (a) and (b) are guide to the eye. (c) Magnetization-dependent anomalous Nernst effect of  $\text{Mn}_3\text{Si}_2\text{Te}_6$  in comparison with various conventional magnetic materials and magnetic topological materials [2,20,25,38–43]. The shaded region represents the case covered by conventional magnets with  $|S_{yx}^A| = |Q_S|\mu_0 M$ ,  $|Q_S| = 0.05 - 1 \mu\text{V K}^{-1} \text{T}^{-1}$ .

more clearly in Fig. 3(b). Below  $T_c$ ,  $S_{xx}(B)$  shows complex behaviors especially in small magnetic fields. The sharp cusp in  $S_{xx}(B)$  near zero field is certainly linked to the metamagnetic transition as seen in magnetization measurements [see Fig. 1(c)]. In both zero magnetic field and 14 T, the Seebeck coefficient increases monotonically with increasing temperature, and no traces of phonon drag are found. This implies that the Seebeck effect is dominated by diffusion effects in which carriers are predominantly scattered by impurities. In the free electron gas scenario, assuming that the relaxation time is energy independent, the diffusion thermoelectric coefficient ( $S_{xx}^d$ ) can be described as the entropy ( $S$ ) per unit charge following the Mott relation, i.e.,  $S_{xx}^d = -S/ne$  [34], where  $n$  is the carrier density,  $e$  is the electronic charge. This simple relation is valid both in zero magnetic field and high magnetic fields [34]. The negative magneto-Seebeck effect is consistent with the negative magnetoresistance, which is likely caused by field-induced suppression (enhancement) of the bandgap (carrier density) [9,14].

Figure 3(c) shows the Nernst effect measured at fixed temperatures. At high temperatures above 200 K, the Nernst signal  $S_{yx} = E_y/\nabla_x T$  depends linearly on magnetic field. Below 150 K, nonlinear magnetic field dependence is seen in  $S_{yx}(B)$ , which becomes more apparent at lower temperatures. Notably, a steplike feature appears near zero magnetic field in the vicinity of  $T_c$ . This feature becomes more pronounced below  $T_c$ . In typical ferromagnets, both the ordinary ( $S_{yx}^N$ ) and anomalous ( $S_{yx}^A$ ) Nernst effects contribute to the total Nernst signal, i.e.,  $S_{yx}(B) = S_{yx}^N + S_{yx}^A$ . In the free-electron approximation, the ordinary Nernst effect dominated by diffusion effects can be obtained via the Mott relation as  $S_{yx}^N = Q_0\mu B/[1 + (\mu B)^2]$ , which scales linearly with magnetic field in the low-field region [34–36]. Here,  $Q_0$  is the ordinary Nernst coefficient,  $\mu$  is the carrier mobility. The anomalous component is simply proportional to the magnetization, i.e.,  $S_{yx}^A = Q_S\mu_0 M$ , where  $Q_S$  is the anomalous Nernst coefficient [25,37]. The total Nernst signal containing the ordinary and anomalous parts can thus be modeled as

$$S_{yx}(B) = S_{yx}^N + S_{yx}^A = Q_0 \frac{\mu B}{1 + (\mu B)^2} + Q_S\mu_0 M. \quad (1)$$

As shown in Fig. 3(c), this simple approach can well describe the Nernst data measured above  $T_c$  [see solid black lines in Fig. 3(c)]. Above 100 K, the Nernst effect is dominated by the ordinary term. The anomalous contribution develops gradually below 100 K [see also Fig. 4(a)], in accordance with the rapid enhancement of the spin correlation length and short-range spin fluctuations below 100 K [13].

Below  $T_c$ , the CMR becomes apparent in the low-field region below 3 T, and the expression in Eq. (1) may not be applicable to account for the total Nernst results. However, as seen in Fig. 3(d), the total Nernst signal  $S_{yx}(B)$  scales nicely with the magnetization  $M(B)$  in the high-field region above 3 T. This indicates that the anomalous Nernst effect dominates in high magnetic fields. In the low-field region below 3 T, excess contributions in addition to  $S_{yx}^A$  have to be considered. The excess term peaks around 1 T, which would lead to an unreasonably large mobility higher than  $1 \text{ m}^2 \text{ V}^{-1} \text{ s}^{-1}$  if the excess term is contributed by  $S_{yx}^N$  using the conventional form displayed in Eq. (1). Still, the excess Nernst signal can arise from  $S_{yx}^N$  due to the unusual CMR appearing in the low-field region. Further study is desired to capture the exact field dependence of the ordinary Nernst effect  $S_{yx}^N(B)$  in the presence of the unusual CMR observed in  $\text{Mn}_2\text{Si}_2\text{Te}_6$ .

The fact that the  $S_{yx}^N$  is negligible in the high-field region may suggest moderate  $S_{yx}^N$  in the low-field region, in conventional scenarios. Then, another possibility of the excess Nernst contribution in the low-field region could be the TNE. The TNE-like term ( $S_{yx}^T$ ) can be obtained by subtracting the anomalous contributions from the total Nernst data if the ordinary term is negligible, i.e.,  $S_{yx}^T = S_{yx} - S_{yx}^A$ . The extracted TNE-like contribution is also plotted in Fig. 3(d) (blue solid lines). Similar to the Hall resistivity, the TNE-like data shows a broad peak around 1 T, pointing to the same origin of the THE and TNE.

In Fig. 4(a), the temperature dependence of different contributions in the Nernst effect extracted in 1 T is shown. The corresponding temperature-dependent coefficients are also plotted in Fig. 4(b). Both coefficients of the ordinary and anomalous Nernst terms change systematically with temperature, suggesting reasonable fitting results. In the paramagnetic state, the ordinary contribution plays major roles. The anomalous component appears below 100 K and becomes dominant

in the ferrimagnetic state. The TNE-like part only arises in the magnetically ordered state, pointing to its intimate correlation with the underlying magnetic structure. Note that the ordinary Nernst effect is certainly underestimated below  $T_c$ , leading to the abrupt jump in  $S_{yx}^N$  as it crosses  $T_c$ . Quantified description of  $S_{yx}^N$  in the low-field region, while accounting for the CMR, is essential to properly address the ordinary Nernst effect below  $T_c$ . Nevertheless, the excess Nernst contribution in the low-field region is intimately tied to the unusual CMR, despite overestimation of the TNE-like contribution.

In Fig. 4(c), we compare the ANE of  $\text{Mn}_3\text{Si}_2\text{Te}_6$ , conventional magnets, and typical magnetic topological materials in a  $S_{yx}^A$ - $M$  diagram. The typical region covered by conventional magnetic systems is marked out in a shaded area. Compared with conventional magnets, the ANE of topological magnetic materials, such as  $\text{Co}_2\text{MnGa}$ ,  $\text{Co}_3\text{Sn}_2\text{S}_2$ ,  $\text{Mn}_3\text{Sn}$ , and  $\text{Fe}_3\text{Sn}_2$ , is significantly enhanced due to contributions from large Berry curvature [2,17,18,18–22,25]. In  $\text{Mn}_3\text{Si}_2\text{Te}_6$ , finite Berry curvature can arise near the Fermi energy ( $E_F$ ) when one of the degenerate nodal-line is raised up to  $E_F$  by aligning the magnetic moments along the  $c$  axis [see Fig. 1(a)] [9,14]. However, unlike the typical topological magnetic materials mentioned above, the ANE of  $\text{Mn}_3\text{Si}_2\text{Te}_6$  falls close to the region spanned by conventional magnets. This implies that the Berry curvature associated with the nodal-line topology only has minor contributions in the ANE of  $\text{Mn}_3\text{Si}_2\text{Te}_6$ .

The TNE-like signal observed in the low-field region below 3 T is also unlikely to be caused by the topological nodal-line structure. In small magnetic fields using the  $B \parallel c$  configuration, the spins only tilt moderately toward the  $c$  axis ( $\sim 33^\circ$  in 4.75 T) as shown by neutron diffraction experiments [13]. In the low-field region, the magnetic moments are far from the polarized state along the  $c$  axis, and the impacts of the nodal-line on transport properties are not expected to be significant. At 70 K and in 1 T, the conductivity and Hall conductivity are  $\sigma_{xx} = 75.36 \Omega^{-1} \text{m}^{-1}$  and  $\sigma_{xy} = 0.12 \Omega^{-1} \text{m}^{-1}$ , respectively. These values fall deeply into the localized hopping region following the phase diagram proposed by Onoda *et al.* [44]. Thus, the contributions from intrinsic Berry curvature are unlikely relevant to the THE-like and TNE-like transport effects of  $\text{Mn}_3\text{Si}_2\text{Te}_6$  observed in the low-field region.

We note that the TNE often appears in skyrmion phases, as typically found in  $\text{MnGe}$ ,  $\text{Gd}_2\text{PdSi}_3$ , and  $\text{Fe}_3\text{Sn}_2$  [24,42,45]. In  $\text{Mn}_3\text{Si}_2\text{Te}_6$ , no traces of skyrmion have been found currently. Nevertheless, a noncollinear magnetic structure is found in the ferrimagnetic state by neutron diffraction experiments [13]. The magnetic space group is found to be  $C2'/c'$ , in which the Mn1 and Mn2 layers are coupled antiferromagnetically but no such constraint is put on the interactions between Mn1 spins. Consequently, a noncollinear spin texture is formed, as shown schematically in the bottom left panel of Fig. 1(a) [13]. The TNE-like signal in  $\text{Mn}_3\text{Si}_2\text{Te}_6$  is very likely produced by the noncollinear magnetic state, in agreement with the fact that the TNE only appears below  $T_c$ . Similar TNE has been found in the conical spiral magnetic phase

of a kagome magnet  $\text{ScMn}_6\text{Sn}_6$  [46]. Notably, the TNE of  $\text{Mn}_3\text{Si}_2\text{Te}_6$  appears in the same magnetic field region (0–3 T) where the CMR effect is most profound. This indicates that the CMR is also coupled closely with the noncollinear magnetic structure [13].

Additional contributions to the Nernst signal can arise from ambipolar transport, in which electronlike and holelike bands are compensated [47–49]. However, the transport properties of  $\text{Mn}_3\text{Si}_2\text{Te}_6$  are dominated by holelike carriers, as we have seen in the Hall resistivity and Seebeck data. Ambipolar transport is unlikely the source of the excess Nernst signal observed in small magnetic fields. Notably, chiral orbital currents (COC) running along edges of  $\text{MnTe}_6$  octahedra within the  $ab$  plane have been proposed in  $\text{Mn}_3\text{Si}_2\text{Te}_6$  [8]. The interactions between COC-induced orbital moments, COC domains, and Mn spins can also explain the unusual CMR [8]. The COC orbital moments break the time-reversal symmetry, and could serve as another prominent channel in producing the TNE-like Nernst signal. This scenario has been theoretically introduced to explain the giant Nernst effect in hole-doped cuprate superconductors and heavy-fermion systems [50]. Further theoretical and experimental studies are desired to verify the existence of COC, and to unravel the links between COC and Nernst effect in  $\text{Mn}_3\text{Si}_2\text{Te}_6$ .

#### IV. CONCLUSIONS

In summary, we have studied electrical transport, thermoelectric Seebeck, and Nernst effects in the ferrimagnetic nodal-line semiconductor  $\text{Mn}_3\text{Si}_2\text{Te}_6$ . The electrical and thermoelectric transport properties are dominated by holelike carriers. In the ferrimagnetic state, CMR is found when external magnetic fields are applied along the magnetic hard  $c$  axis. Moreover, the ANE dominates in the Nernst effect in the magnetically ordered state. In addition, possible TNE arises below  $T_c$  in the low-field region where the CMR is most pronounced. It is found that the nodal-line topology plays subdominant roles in the ANE, and the THE-like signal is most likely stemming from the noncollinear magnetic structure of  $\text{Mn}_3\text{Si}_2\text{Te}_6$ .

#### ACKNOWLEDGMENTS

This work has been supported by the National Natural Science Foundation of China (Grants No. 52125103, No. 52071041, No. 12004254, No. 12004056, No. 11974065, and No. 12104254), Chongqing Research Program of Basic Research and Frontier Technology, China (Grant No. cstc2020jcyj-msxmX0263), Chinesisch-Deutsche Mobilitätsprogramm of Chinesisch-Deutsche Zentrum für Wissenschaftsförderung (Grant No. M-0496), The Fundamental and Applied Fundamental Research Grant of Guangdong Province (Grant No. 2021B1515120015), the ninth batch of innovation and entrepreneurship leading talents (innovation category) in 2019, Guangdong Natural Science Funds for Distinguished Young Scholar (2021B1515020101), and Guangdong Natural Science Funds for Distinguished Young Scholar (No. 2021B1515020101).

- [1] Y. Tokura, K. Yasuda, and A. Tsukazaki, *Nat. Rev. Phys.* **1**, 126 (2019).
- [2] M. Ikhlas, T. Tomita, T. Koretsune, M.-T. Suzuki, D. Nishio-Hamane, R. Arita, Y. Otani, and S. Nakatsuji, *Nat. Phys.* **13**, 1085 (2017).
- [3] E. Liu, Y. Sun, N. Kumar, L. Muechler, A. Sun, L. Jiao, S.-Y. Yang, D. Liu, A. Liang, Q. Xu, J. Kroder, V. Süß, H. Borrmann, C. Shekhar, Z. Wang, C. Xi, W. Wang, W. Schnelle, S. Wirth, Y. Chen *et al.*, *Nat. Phys.* **14**, 1125 (2018).
- [4] Y. Deng, Y. Yu, M. Z. Shi, Z. Guo, Z. Xu, J. Wang, X. H. Chen, and Y. Zhang, *Science* **367**, 895 (2020).
- [5] J.-X. Yin, W. Ma, T. A. Cochran, X. Xu, S. S. Zhang, H.-J. Tien, N. Shumiya, G. Cheng, K. Jiang, B. Lian, Z. Song, G. Chang, I. Belopolski, D. Multer, M. Litskevich, Z.-J. Cheng, X. P. Yang, B. Swidler, H. Zhou, H. Lin *et al.*, *Nature (London)* **583**, 533 (2020).
- [6] S. Nakatsuji and R. Arita, *Annu. Rev. Condens. Matter Phys.* **13**, 119 (2022).
- [7] Y. Ni, H. Zhao, Y. Zhang, B. Hu, I. Kimchi, and G. Cao, *Phys. Rev. B* **103**, L161105 (2021).
- [8] Y. Zhang, Y. Ni, H. Zhao, S. Hakani, F. Ye, L. DeLong, I. Kimchi, and G. Cao, *Nature (London)* **611**, 467 (2022).
- [9] J. Seo, C. De, H. Ha, J. E. Lee, S. Park, J. Park, Y. Skourski, E. S. Choi, B. Kim, G. Y. Cho *et al.*, *Nature (London)* **599**, 576 (2021).
- [10] J. Wang, S. Wang, X. He, Y. Zhou, C. An, M. Zhang, Y. Zhou, Y. Han, X. Chen, J. Zhou, and Z. Yang, *Phys. Rev. B* **106**, 045106 (2022).
- [11] A. F. May, Y. Liu, S. Calder, D. S. Parker, T. Pandey, E. Cakmak, H. Cao, J. Yan, and M. A. McGuire, *Phys. Rev. B* **95**, 174440 (2017).
- [12] G. Sala, J. Y. Y. Lin, A. M. Samarakoon, D. S. Parker, A. F. May, and M. B. Stone, *Phys. Rev. B* **105**, 214405 (2022).
- [13] F. Ye, M. Matsuda, Z. Morgan, T. Sherline, Y. Ni, H. Zhao, and G. Cao, *Phys. Rev. B* **106**, L180402 (2022).
- [14] Y. Zhang, L.-F. Lin, A. Moreo, and E. Dagotto, *Phys. Rev. B* **107**, 054430 (2023).
- [15] D. Xiao, M.-C. Chang, and Q. Niu, *Rev. Mod. Phys.* **82**, 1959 (2010).
- [16] D. Xiao, Y. Yao, Z. Fang, and Q. Niu, *Phys. Rev. Lett.* **97**, 026603 (2006).
- [17] S. N. Guin, P. Vir, Y. Zhang, N. Kumar, S. J. Watzman, C. Fu, E. Liu, K. Manna, W. Schnelle, J. Gooth *et al.*, *Adv. Mater.* **31**, 1806622 (2019).
- [18] H. Yang, W. You, J. Wang, J. Huang, C. Xi, X. Xu, C. Cao, M. Tian, Z.-A. Xu, J. Dai, and Y. Li, *Phys. Rev. Mater.* **4**, 024202 (2020).
- [19] L. Ding, J. Koo, L. Xu, X. Li, X. Lu, L. Zhao, Q. Wang, Q. Yin, H. Lei, B. Yan, Z. Zhu, and K. Behnia, *Phys. Rev. X* **9**, 041061 (2019).
- [20] S. N. Guin, K. Manna, J. Noky, S. J. Watzman, C. Fu, N. Kumar, W. Schnelle, C. Shekhar, Y. Sun, J. Gooth *et al.*, *NPG Asia Mater.* **11**, 16 (2019).
- [21] L. Xu, X. Li, L. Ding, T. Chen, A. Sakai, B. Fauqué, S. Nakatsuji, Z. Zhu, and K. Behnia, *Phys. Rev. B* **101**, 180404 (2020).
- [22] A. Sakai, Y. P. Mizuta, A. A. Nugroho, R. Sihombing, T. Koretsune, M.-t. Suzuki, N. Takemori, R. Ishii, D. Nishio-Hamane, R. Arita, P. Goswami, and S. Nakatsuji, *Nat. Phys.* **14**, 1119 (2018).
- [23] X. Li, L. Xu, L. Ding, J. Wang, M. Shen, X. Lu, Z. Zhu, and K. Behnia, *Phys. Rev. Lett.* **119**, 056601 (2017).
- [24] H. Zhang, C. Q. Xu, and X. Ke, *Phys. Rev. B* **103**, L201101 (2021).
- [25] Y. Li, J. Zhou, M. Li, L. Qiao, C. Jiang, Q. Chen, Y. Li, Q. Tao, and Z.-A. Xu, *Phys. Rev. Appl.* **19**, 014026 (2023).
- [26] J. Xu, W. A. Phelan, and C.-L. Chien, *Nano Lett.* **19**, 8250 (2019).
- [27] See Supplemental Material at <http://link.aps.org/supplemental/10.1103/PhysRevB.108.125103> for crystal characterizations and more experimental data.
- [28] Y. Liu, Z. Hu, M. Abeykoon, E. Stavitski, K. Attenkofer, E. D. Bauer, and C. Petrovic, *Phys. Rev. B* **103**, 245122 (2021).
- [29] A. F. May, H. Cao, and S. Calder, *J. Magn. Magn. Mater.* **511**, 166936 (2020).
- [30] S. Djurdjic Mijin, A. Šolajić, J. Pešić, Y. Liu, C. Petrovic, M. Bockstedte, A. Bonanni, Z. V. Popović, and N. Lazarević, *Phys. Rev. B* **107**, 054309 (2023).
- [31] P. K. Rout, P. V. P. Madduri, S. K. Manna, and A. K. Nayak, *Phys. Rev. B* **99**, 094430 (2019).
- [32] Z. H. Liu, Y. J. Zhang, G. D. Liu, B. Ding, E. K. Liu, H. M. Jafri, Z. P. Hou, W. H. Wang, X. Q. Ma, and G. H. Wu, *Sci. Rep.* **7**, 515 (2017).
- [33] C. Stürgers, G. Fischer, P. Winkel, and H. V. Löhneysen, *Nat. Commun.* **5**, 3400 (2014).
- [34] R. Fletcher, *Semicond. Sci. Technol.* **14**, R1 (1999).
- [35] T. Liang, J. Lin, Q. Gibson, T. Gao, M. Hirschberger, M. Liu, R. J. Cava, and N. P. Ong, *Phys. Rev. Lett.* **118**, 136601 (2017).
- [36] T. Liang, Q. Gibson, J. Xiong, M. Hirschberger, S. P. Koduvayur, R. Cava, and N. Ong, *Nat. Commun.* **4**, 2696 (2013).
- [37] W.-L. Lee, S. Watauchi, V. L. Miller, R. J. Cava, and N. P. Ong, *Phys. Rev. Lett.* **93**, 226601 (2004).
- [38] R. Ramos, M. H. Aguirre, A. Anadón, J. Blasco, I. Lucas, K. Uchida, P. A. Algarabel, L. Morellón, E. Saitoh, and M. R. Ibarra, *Phys. Rev. B* **90**, 054422 (2014).
- [39] K. Hasegawa, M. Mizuguchi, Y. Sakuraba, T. Kamada, T. Kojima, T. Kubota, S. Mizukami, T. Miyazaki, and K. Takanashi, *Appl. Phys. Lett.* **106**, 252405 (2015).
- [40] N. Hanasaki, K. Sano, Y. Onose, T. Ohtsuka, S. Iguchi, I. Kézsmárki, S. Miyasaka, S. Onoda, N. Nagaosa, and Y. Tokura, *Phys. Rev. Lett.* **100**, 106601 (2008).
- [41] J. Weischenberg, F. Freimuth, S. Blügel, and Y. Mokrousov, *Phys. Rev. B* **87**, 060406 (2013).
- [42] Y. Shiomi, N. Kanazawa, K. Shibata, Y. Onose, and Y. Tokura, *Phys. Rev. B* **88**, 064409 (2013).
- [43] K.-I. Uchida, T. Kikkawa, T. Seki, T. Oyake, J. Shiomi, Z. Qiu, K. Takanashi, and E. Saitoh, *Phys. Rev. B* **92**, 094414 (2015).
- [44] S. Onoda, N. Sugimoto, and N. Nagaosa, *Phys. Rev. B* **77**, 165103 (2008).
- [45] M. Hirschberger, L. Spitz, T. Nomoto, T. Kurumaji, S. Gao, J. Masell, T. Nakajima, A. Kikkawa, Y. Yamasaki, H. Sagayama,

- H. Nakao, Y. Taguchi, R. Arita, T.-H. Arima, and Y. Tokura, *Phys. Rev. Lett.* **125**, 076602 (2020).
- [46] R. P. Madhugaria, S. Mozaffari, H. Zhang, W. R. Meier, S.-h. Do, R. Xue, T. Matsuoka, and D. G. Mandrus, [arXiv:2305.06496](https://arxiv.org/abs/2305.06496).
- [47] R. T. Delves, *Rep. Prog. Phys.* **28**, 249 (1965).
- [48] R. Bel, K. Behnia, and H. Berger, *Phys. Rev. Lett.* **91**, 066602 (2003).
- [49] Y. Gan, W. Xia, L. Zhang, K. Yang, X. Mi, A. Wang, Y. Chai, Y. Guo, X. Zhou, and M. He, *Phys. Rev. B* **104**, L180508 (2021).
- [50] P. Kotetes and G. Varelogiannis, *Phys. Rev. Lett.* **104**, 106404 (2010).